LASER & PHOTONICS REVIEWS
www.lpr-journal.org

Ultra-Flat Broadband Low-Noise Frequency Comb in a Fiber Fabry-Perot Resonator

*Tieying Li, Jianping Chen, and Kan Wu**

A low-noise microcomb with a flat and broadband spectrum is highly desired for various applications, including spectroscopy, sensing, and communications. However, both dissipative Kerr solitons (DKSs) and platicons have limitations in spectrum flatness due to their sech-shaped profile or peaks of dispersive waves. In this study, an ultra-flat and broadband microcomb are presented in a fiber Fabry-Perot (F-P) resonator. By optimizing the group velocity dispersion (GVD) and third-order dispersion (TOD), an ultra-flat low-noise comb spectrum is obtained with a −1 dB bandwidth of up to 58 nm and a −30 dB bandwidth of 190 nm. Additionally, a method to control the contribution of the stimulated Raman scattering (SRS) effect by adjusting the desynchronization frequency to meet the phase-matching condition is proposed. With the contribution from SRS, the −30 dB bandwidth is further extended to 230 nm with more than 7700 comb lines. Furthermore, a detailed investigation is conducted on the interaction among GVD, TOD, SRS, and Kerr nonlinearity, revealing the generation mechanism of such an ultra-flat broadband comb spectrum. The work will provide valuable insights for the advancement of dispersion-engineered resonators and further stimulate the study of the effects of SRS in fiber and integrated resonators are anticipated.

1. Introduction

Due to the small mode volume and high Q-factor of the microcavity, the inside light field is significantly enhanced, resulting in a variety of nonlinear optical phenomena. One such phenomenon is the presence of dissipative solitons,[1] which are stable temporal structures capable of propagating within the cavity while preserving their shape and energy. The formation of these structures relies on a delicate balance between losses and gains, as well as between nonlinearity and dispersion.[2] Dissipative Kerr solitons (DKSs) are commonly observed in two main platforms: fiber ring resonators[3–5] (or Fabry-perot (F-P) resonator[6–9]) and microresonators made of different materials, including MgF_2,[1] Si_3N_4,[10,11] silicon,[12] silica,[13,14] $LiNbO_3$,[15–17] and AlN,[18,19] AlGaAs.[20]

In order to generate DKSs, it is essential that group velocity dispersion (GVD) is anomalous. However, in the near-infrared range, most materials exhibit normal GVD, necessitating the introduction of additional waveguide dispersion. These sech-shaped DKSs, located in the red-detuned region of the bistable curve,[21] face two primary challenges: low conversion efficiency[22,23] and thermal instability.[24–26] As a result, an amount of theory[27,28] and experiments[29–38] have been devoted to exploring dark solitons in the normal GVD regime due to their highly efficient conversion[39] and stability within the blue region of the bistable curve. The flat-top soliton called platicon,[40–42] which is considered a high-order dark soliton, is formed through the interaction between two switching waves[27] near the Maxwell point in the normal GVD regime. When the GVD ≈0, the influence of third-order dispersion (TOD) becomes significant.[27] This leads to the oscillations at the peak of the switching waves, naturally allowing for the locking of switching waves and the generation of bright solitons.[28,43]

Experiments conducted using fiber ring resonators[44] or Si_3N_4[45] microresonators have confirmed the existence of these bright solitons called zero dispersion solitons when operating in a regime of closing zero GVD. However, the fiber ring-generated microcombs[44] exhibit a relatively narrow bandwidth (30 nm at a −30 dB threshold from the pump line to the combs). Although Si_3N_4 microresonators[45] generated microcombs can offer a broader spectral bandwidth (20 THz at a −30 dB threshold), the high repetition frequency (~22 GHz) may not be suitable for some applications that require lower repetition frequencies (1–10 GHz).[46,47] Both studies[44,45] have observed significant power fluctuations in the spectra, with substantial variations of ~10 dB. These problems raise a natural question of whether it is possible to achieve a broadband, ultra-flat, GHz-level microcomb. Recent experimental advancements have demonstrated the existence of dispersion-less Nyquist solitons[48] with an ultra-flat spectrum through the combination of normal GVD and spectral filtering. However, the attainable spectral bandwidth remains limited to ≈250 GHz (≈2 nm). A recent study[49] reported on a

T. Li, J. Chen, K. Wu
State Key Laboratory of Advanced Optical Communication Systems and Networks
School of Electronic Information and Electrical Engineering
Department of Electronic Engineering
Shanghai Jiao Tong University
Shanghai 200240, China
E-mail: kanwu@sjtu.edu.cn

The ORCID identification number(s) for the author(s) of this article can be found under https://doi.org/10.1002/lpor.202400180

DOI: 10.1002/lpor.202400180

soliton comb featuring a repetition frequency of 48.9 GHz and a −10 dB bandwidth of 150 nm, achieved through dispersion optimization. However, an additional bandstop filter may be needed to filter the pump.

Stimulated Raman scattering (SRS) is a crucial nonlinear optical process, particularly in the generation of supercontinuum spectra using nonlinear optical fibers. Recent studies have highlighted its significant influence on the production of Raman lasers[50,51] or Raman frequency combs[52–54] in microresonators. In the anomalous GVD regime, SRS can alter the dynamics of DKSs[55–58] or facilitate the emergence of novel solitons, such as Stokes solitons.[59,60] Under normal GVD conditions, SRS can affect the spatiotemporal stability of platicons,[61] or give rise to Raman solitons[62] and SRS-enabled localized structure.[63,64] In comparison to the limited gain region of Brillouin scattering,[65] SRS in silica can provide a broader gain region with a down-frequency shift of ~13 THz. Recent research[64] suggests that the (DW) can act as a seed and be amplified by SRS with negligible TOD, thus broadening the spectrum. But it is still unknown about the comb evolution if there is no seed of DW while the combs are still located in the Raman gain region. The works[4,62] discuss the generation of the Raman soliton by setting the pump and the center wavelength of the Raman soliton at two phase-matching points of the phase-matching curve. However, the requirement for efficiently exciting SRS in the normal GVD regime remains unclear and the experimental study on the interaction among SRS, GVD, and TOD is also lacking.

In this paper, we present an F-P resonator platform that not only permits the generation of ultra-flat and broadband comb spectrum but also allows manual control of the contribution of the SRS effect by adjusting the phase-matching condition to investigate the interaction between SRS and other effects. The key consideration to flatten the spectrum is to balance the influence of normal GVD and TOD. A relatively large normal GVD ensures that the center of the spectrum exhibits a platicon-like shape, while also allowing the influence of TOD to extend the spectrum. In the time domain, the combined effects of GVD and TOD lead to a bright structure (BS) that exhibits a significant number of peaks atop the pulse. The number of peaks surpasses that of near-zero-dispersion solitons, leading to a reduction in amplitude modulation in the spectrum and resulting in a flattened spectrum. We have successfully experimentally achieved an ultra-flat, broadband, and low-noise comb spectrum with a −1 dB bandwidth of 58 nm and a −30 dB bandwidth of 190 nm. When the phase matching condition for SRS is achieved by adjusting the desynchronization frequency, the influence of SRS is stimulated and the spectrum is broadened with a −30 dB bandwidth of 230 nm, but at the expense of reduced flatness. (−1 dB bandwidth reduced to 16 nm). Detailed simulation and experiment have also been performed to reveal the mechanism of generating the ultra-flat and broadband comb spectrum as well as the mutual interaction among GVD, TOD, SRS, and Kerr nonlinearity. This work provides a route to achieve an ultra-flat, broadband, and low-noise comb spectrum and a method to manually control the contribution of SRS, which can stimulate the application of the flat microcombs and the research on the mutual interaction between SRS and various effects in both fiber and integrated resonators.

2. Theory and Simulation

Figure 1a presents a schematic diagram that illustrates the output spectrum of the F-P resonator. In Figure 1b, the photo of the resonator is also depicted. A pulsed pumping technique is employed to stimulate the FP cavity.[66] The upper spectrum in Figure 1a represents the output of an ultra-flat BS spectrum with normal GVD and TOD. The lower spectrum in Figure 1b represents the broadened spectrum with enhanced SRS effect by adjusting the frequency difference between the pump repetition rate and the natural rate of the FP cavity (referred to as the desynchronization frequency δf_{eo}). This adjustment enables the amplification of SRS, leading to an expansion of the BS spectrum and the generation of the SRS-amplified BS (SRS-BS) spectrum.

In our system, SRS refers to the interaction between pump photons (with energy $\hbar\omega_p$) and the silica molecules within the fiber. This interaction generates low-frequency scattered photons, known as Stokes photons ($\hbar\omega_s$), and phonons ($\hbar\Omega_R$) which correspond to the molecular vibration frequency. The energy level schematic of SRS is depicted in Figure 1c. The energy of the pump is nonlinearly transferred to the lower frequency spectrum. The Raman gain demonstrates broad spectral characteristics due to the formation of molecular vibration energy bands within the amorphous silica structure of the fiber.

To analyze the dynamic evolution of the optical field under the influence of SRS, GVD, TOD, and Kerr nonlinearity at various desynchronization frequencies, our study begins with the widely recognized Lugiato-Lefever equation (LLE) as follows[67]:

$$\begin{aligned}\frac{\partial A(t,\tau)}{\partial t} &= \mathcal{F}\left[i\left(\delta\omega+\mu\cdot 2\pi\delta f_{eo}+D_{int}(\mu)\right)\tilde{A}_{\mu}\right]-\frac{\kappa}{2}A\\ &\quad+ig\left((1-f_R)\left(|A|^2+2\left\langle|A|^2\right\rangle\right)+f_R h_R(\tau)*|A|^2\right)A\\ &\quad+\sqrt{\frac{\kappa_{ex}P_0}{\hbar\omega_0}}f_P(\tau)\end{aligned} \tag{1}$$

Where t represents the slow time and τ represents the fast time. The intra-cavity photon field is denoted as $A(t,\tau)$, $\delta\omega$ refers to the detuning between the pump combs and the nearest resonance modes, while δf_{eo} represents the mismatch between the pump repetition rate and the FSR of the cavity. $D_{int} = \mu^2/2\cdot D_2+\mu^3/6\cdot D_3+\cdots$ describes the linear phase operator that accounts for cavity dispersion, including the GVD coefficient (D_2), the TOD coefficient (D_3), and higher-order terms. μ corresponds to the number of resonance modes. The loss rate κ encompasses the coupling rate κ_{ex} and the intrinsic loss rate κ_0. The nonlinear coupling coefficient is denoted as g, and f_R represents the Raman fraction. P_0 is the peak power of the pulse function $f_p(\tau)$. The average intracavity photon flux over the time domain is denoted as $\langle|A|^2\rangle$, with τ_R representing the round-trip time.

$$\left\langle|A|^2\right\rangle=\frac{1}{\tau_R}\int_{-\tau_R/2}^{\tau_R/2}|A(t,\tau)|^2\,d\tau \tag{2}$$

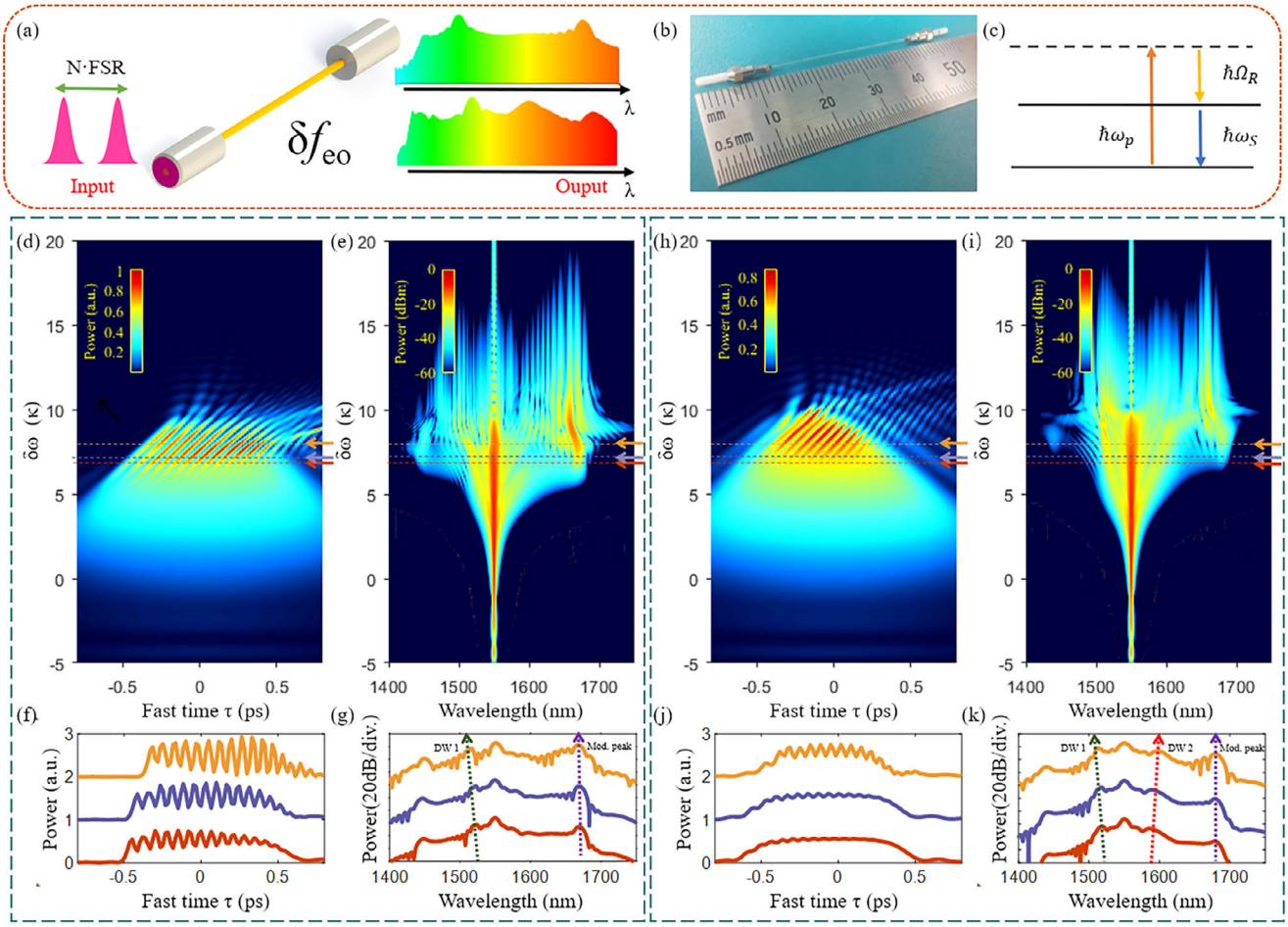

Figure 1. Simulation of the BS formation. a) Illustration of the generation of two different spectra through adjusting δf_{eo} in a fiber F-P resonator, when considering GVD, TOD, and SRS effects. b) Photo of the F-P resonator. c) Energy level schematic of the SRS. The temporal profile d) and spectrum e) evolution of the intra-cavity fields versus the detuning $\delta\omega$ when $\delta f_{eo} = -10$ kHz. The red, blue, and yellow arrows correspond to $\delta\omega$ values of 6.9 κ, 7.2 κ, and 8.0 κ. The corresponding f) temporal waveforms and g) spectra are indicated by the arrows in (d) and (e). In (g), as the detuning increases. The dotted green and purple lines represent the movement of dispersive wave 1 (DW 1) near 1510 nm and the modulated peak near 1670 nm, respectively. (h-k) Temporal and spectral evolution of the intracavity fields with the same parameters as (d-g) except $\delta f_{eo} = 5$ kHz. In (k), the dotted green, red, and purple lines represent the movement of DW 1, DW 2, and the modulated (mod.) peak, respectively.

The SRS term is characterized by the corresponding temporal function, $h_R(\tau)$, expressed as:

$$h_R(\tau) = \frac{\tau_1^2 + \tau_2^2}{\tau_1 \tau_2^2} e^{-\tau/\tau_2} \sin(\tau/\tau_1) \tag{3}$$

The simulated and experimental parameters are available in Appendix.

A Gaussian pulse, $f_p(\tau)$, defined as $P_0 \exp(-\tau^2/\tau_p{}^2)$, is used as the pumping source. The pulse has a duration τ_p of 1.1 ps and a peak power P_0 of 13 W. To observe the dynamics of the intra-cavity optical field, we conduct a linear scan of the detuning $\delta\omega$, ranging from -5 κ to 20 κ, i.e., from the blue to the red detuning. δf_{eo} is a crucial parameter for determining the emission position of dispersive waves, as described by the equation[4]: $D_{int}+\mu\bullet 2\pi\bullet\delta f_{eo} = 2\bullet\gamma\bullet P\bullet L\bullet\text{FSR}\text{-}\delta\omega = \delta\omega_{eff}$, where P represents the peak power of the intracavity pulse, $\gamma = (2\pi g n_0) / (\hbar\omega_p D_1 c)$ is the nonlinear coefficient. By adjusting δf_{eo}, we can tune the emission position of the DW and align it with the Raman gain region to enhance the SRS contribution.

In the first simulation scenario, we set δf_{eo} to -10 kHz, ensuring the absence of a DW in the Raman gain region. Consequently, the evolution of the intra-cavity field primarily depends on GVD ($D_2/2\pi = -31.7$ Hz) and TOD ($D_3/2\pi = -48.29$ mHz). The temporal and frequency domain evolutions are depicted in Figure 1d,e, respectively. In the range of detuning scanned from 3 to 5.7 κ, the intra-cavity field exhibits the conventional platicon state. During this stage, as the detuning increases, the temporal width of the intra-cavity field narrows while the spectrum expands. When the detuning exceeds 5.7 κ, the top of the platicon is affected by TOD, resulting in oscillations and forming a BS. Figure 1f presents the typical temporal structure of the BS under three different detuning as 6.9, 7.2, and 8.0 κ. It is evident that the number of oscillations on the top significantly exceeds that of zero-dispersion solitons due to the significantly larger GVD

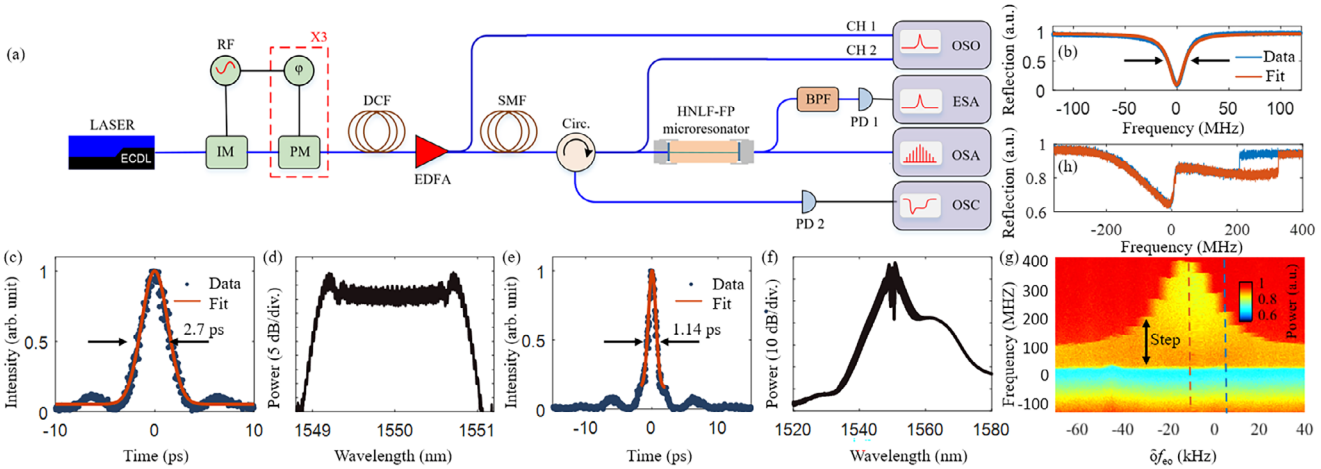

Figure 2. Experimental generation of the BS and the SRS-BS combs. a) Experimental setup. IM: intensity modulator; PM: phase modulators; Φ: phase shifter; DCF: dispersion compensating fiber; SMF: single mode fiber; EDFA: erbium-doped fiber amplifier; OSO: optical sampling oscilloscope; PD: photodetector; BPF: bandpass filter; OSC: oscilloscope; ESA: electrical spectrum analyzer; OSA: optical spectrum analyzer; b) Cold cavity resonance. c) Temporal waveform and d) spectrum of the initial pump pulse. e) Temporal waveform and f) spectrum of the nonlinearly compressed pulse. g) Resonance reflection with step-like feature at different δf_{eo} values. Red line for $\delta f_{eo} = -10$ kHz and blue line for $\delta f_{eo} = 5$ kHz. (h) Detailed step feature at $\delta f_{eo} = -10$ kHz (red line) or 5 kHz (blue line).

compared to the zero-dispersion solitons.[44,45] This larger GVD allows for a wider pulse width, thereby facilitating the existence of more oscillations. As shown in Figure 1g, in the frequency domain, the BS spectrum exhibits a distinctive platicon comb centered around two prominent peaks. The left peak corresponds to the dispersive wave 1 (DW 1), which shifts toward shorter wavelengths as the detuning increases (see dotted green line). The right peak near 1670 nm arises from TOD, which induces oscillatory tails of the up-switching wave and the oscillation period determines the position of this peak.[28] We name this peak as the modulated peak. The modulated peak slowly shifts toward shorter wavelengths with the increasing detuning but the shift is negligible when the detuning $\delta\omega$ is below 8.3 κ (see dotted purple line). A simulation investigation on the influence of GVD, TOD, and pump power on this modulated peak is provided in Section S1 (Supporting Information). The peak near 1450 nm is obtained by the degenerate four-wave mixing (FWM) between the pump and the modulated peak. At a detuning of 6.9 κ, the spectrum demonstrates exceptional flatness. It is noted that the ultra-flat spectrum observed does not depend on the Raman response (see Section S2, Supporting Information). As the detuning increases, both the number and amplitude of oscillations on the BS increase, resulting in a decrease in spectral flatness. The whole evolution of the temporal profiles and spectra at different detuning can be seen in the supplemental GIF1.

In the second simulation scenario, the detuning parameter (δf_{eo}) is set to +5 kHz. The temporal and frequency domain evolutions are illustrated in Figure 1h,i, respectively. The spectra at three detunings 6.9, 7.2, and 8.0 κ are also shown in Figure 1k, where three peaks are observed: DW 1, DW 2, and the modulated peak. DW 1 and the modulated peak exhibit similar behavior as observed in the first scenario, while DW 2 is a newly introduced peak that shifts toward longer wavelengths as the detuning increases (see dotted red line). It is important to note that DW 2 holds significant importance for expanding the BS spectrum. Although DW 2 is located ≈1590 nm, it does not align with the gain region of the silica fiber in the theoretical model (≈1650 nm). However, it is close to the wavelength used in the following experiment involving erbium-doped fiber at ≈1612 nm. This discrepancy in the wavelength of the gain region can be attributed to the influence of the doped rare-earth ions in the erbium-doped fiber, which results in a shift in the location of the Raman gain region. The development of a comprehensive Raman model for erbium-doped fiber presents a challenging task, which has limited the observation of the Stokes peak through the simulation. The entire evolution of the temporal profiles and spectra can be referred to in the supplemental GIF2.

3. Experimental Setup

The Fabry-Perot cavity used in the experiment, as shown in Figure 1b, has a length of ≈5 cm. The cavity comprises a ceramic sleeve housing a low-concentration erbium-doped fiber (EDF3/6/125-23, YOFC). The fiber end faces are polished and coated with high reflectivity films, consisting of 25 pairs of SiO_2 and Ta_2O_5. These films form Bragg mirrors with a reflectivity of up to 99.6%. Due to their minimal film absorption and fiber transmission loss (≈3.5 dB m^{-1} at 1530 nm, will be bleached by pump), the resonator linewidth is measured to be 19 MHz (refer to **Figure** 2b), corresponding to a loaded Q factor of 1×10^7. The usage of such a fiber is to utilize its relatively small Raman frequency (near 1612 nm for 1550 nm pump, see Section S3, Supporting Information) to match the DW in our experiment. The erbium ions are bleached under pulsed pumping and do not affect the comb formation.

The dispersion of the fiber is measured using the Mach-Zehnder interferometer (MZI) method.[64] The measured value of GVD is 1.6 ps^2 km^{-1}, corresponding to $D_2/2\pi = -28.2 \pm 3$ Hz. The measured TOD value is 0.1095 ps^3 km^{-1}, corresponding to $D_3/2\pi = -44.8 \pm 5$ mHz. The value of δf_{eo} is determined using the formula $2 \times \text{FSR}\text{-}f_{eo}$. Here, f_{eo} refers to the frequency of the RF source while FSR represents the intrinsic frequency of the

F-P cavity. To precisely determine the intrinsic frequency of the F-P cavity, a dual-cavity method is utilized,[68] resulting in a 2nd harmonic (2 × FSR) value of 3.695923 GHz. In order to reduce the impact of external stress and temperature fluctuations on the FP resonator, a specially designed copper fixture with a thermoelectric cooler (TEC) is utilized to enclose the entire F-P resonator.

The entire experimental setup is illustrated in **Figure** 2a The intensity modulator, along with three-phase modulators, is employed to modulate the tunable single-frequency laser, generating an electro-optic (EO) frequency comb. To compensate for the dispersion of the EO frequency comb, dispersion compensation fiber (DCF) is utilized, producing pump pulses with a repetition frequency of ≈3.6 GHz, which is approximately twice the intrinsic rate of the F-P resonator.[66] The temporal profile of the pump pulse is measured using an optical sampling oscilloscope (OSO, Alnair Labs EYE-2000C, >500 GHz bandwidth). Figure 2c presents the temporal profile of the pump pulse, exhibiting a pulse width of 2.70 ps. The pulse spectrum comprises 53 frequency comb lines within the −10 dB range (Figure 2d). To enhance the peak power of the pump pulse, a 100-meter-long single-mode fiber (SMF) is employed for nonlinear pulse compression. Before entering the SMF, the power of the pump pulse is amplified to 28 dBm using an erbium-doped fiber amplifier (EDFA). The pulse width is compressed from 2.70 to 1.14 ps (Figure 2e), and the −30 dB bandwidth is increased from 2 nm (Figure 2d) to 25 nm (Figure 2f). The optical power before entering the FP cavity is measured as 23 dBm and the estimated power coupled to the FP microcavity is 18 dBm, accounting for fiber optic connection loss.

In order to investigate the nonlinear response of the field within the F-P cavity and the influence of δf_{eo}, we conducted a rapid scanning at a speed of 58 GHz/s. The scanning range extends from the blue-detuned region to the red-detuned region, and the power of the reflected light from the F-P cavity is detected through photodetector 2 (PD 2). As depicted in Figure 2g, we observed the presence of soliton steps within the δf_{eo} range of −50 to 50 kHz. The soliton step reaches its maximum length of 300 MHz when δf_{eo} is −10 kHz, as indicated by the red line in Figure 2h. Additionally, a shorter step length of 200 MHz is observed when δf_{eo} is 5 kHz, as shown by the blue line in Figure 2h. In the experiment, we initially set the values of δf_{eo} to −10 kHz, which resulted in an ultra-flat BS spectrum. Subsequently, we adjusted δf_{eo} to +5 kHz to observe an expanded BS spectrum, referred to as the SRS-BS spectrum and analyzed the interactions among SRS, GVD, and TOD.

4. Experimental Observation of (BS)

In order to monitor the real-time variations of the optical field during the laser scanning process, a computer program is employed to control the laser frequency. The laser frequency is adjusted at a rate of 1.2 MHz s^{-1}. After each frequency adjustment, an optical spectrum analyzer (OSA) is utilized to record the transmission spectrum of the F-P cavity, while a photodetector (PD 2) is employed to measure the reflected optical power of the F-P cavity. This approach is feasible due to the reduced thermal effects resulting from the lower average pump power of the pulsed pump, and the presence of optical combs within the effective blue detuning region of normal dispersion.

The detuning frequency (δf_{eo}) is first adjusted to −10 kHz in order to generate an ultra-flat BS spectrum. Figure illustrates the spectra obtained by gradually increasing the detuning (decreasing the laser frequency). The vertical axis in the figure represents the absolute frequency deviation of the laser from its initial position (0 MHz), rather than the detuning relative to the resonance mode. When the detuning is tuned to 41 MHz, the spectrum experiences noticeable broadening. Simultaneously, the reflected curve exhibits distinctive step-like characteristics, with a step length of ≈118 MHz (see Section S4, Supporting Information). The formation of this step is attributed to the sudden increase in pump power coupled to the resonance, resulting in a decrease in the reflected pump power.

The process of detuning is examined using three distinct values: 122.7 MHz, 146.2 MHz, and 157.8 MHz, which correspond to the red, blue, and green dotted lines in **Figure** 3a and solid lines in Figure 3c. The BS spectra display a centered platicon spectrum with two distinct peaks named DW 1 (marked by the green arrow in Figure 3c) and modulated peak (marked by the purple arrow). As the detuning increased, DW 1 shifted toward shorter wavelengths, see the dot green arrow in Figure 3c. The position of DW 1 can be determined by the formula $D_{int}+\mu\cdot 2\pi\cdot\delta f_{eo} = 2\cdot\gamma\cdot P\cdot L\cdot\text{FSR}\cdot\delta\omega = \delta\omega_{\text{eff}}$, where $\delta\omega_{\text{eff}}$ is obtained by using live cavity phase response measurements (see Section S5, Supporting Information). The position of DW 1 is marked by the green dot in Figure 3b, which aligns with the measured positions of DW 1 of the red line in Figure 3c. In contrast, the wavelength of the modulated peak remains nearly constant at 1670 nm regardless of changes in detuning (see the purple arrow), which is consistent with the simulation analysis. The simulation spectra for the three different detuning values are depicted as the yellow lines in Figure 3c, showing good agreement with the experimental results. When the detuning is 122.7 MHz, the BS spectrum (indicated by the red line in Figure 3c) exhibits a wide bandwidth and excellent flatness. The spectrum has a flat −3 dB bandwidth up to 78 nm from 1574 to 1652 nm and an ultra-flat −1 dB bandwidth up to 58 nm from 1586 to 1644 nm (see Figure 3e). The spectrum also has a wide −30 dB bandwidth of 190 nm spanning from 1504 to 1694 nm. The comb spacing is ∼3.69 GHz and the number of comb lines is greater than 1800 (−1 dB). The simulated temporal profile is shown in the bottom line of Figure 3d. The temporal profile shows weak oscillations with a period of 0.07 ps. The oscillation has a duty cycle of ∼50% and can simply be considered a sinusoidal modulation whose period determines the position of the carrier frequency (i.e., the position of the modulated peak). This period corresponds to a frequency interval of 1/0.07 ps = 14.2 THz, which matches well with the experimentally measured spectral interval of 13.9 THz (1550 nm to 1670 nm). Increasing the detuning to 146.2 and 157.8 MHz (as shown in Figure 3d middle and top lines) results in an increase in both the amplitude and number of oscillations, while the flatness of the spectra deteriorates (see blue and green lines in Figure 3c). The BS spectrum's bandwidth can also be adjusted by varying δf_{eo}. The −30 dB bandwidths can be adjusted in a range from 190 to 140 nm (see Section S6, Supporting Information).

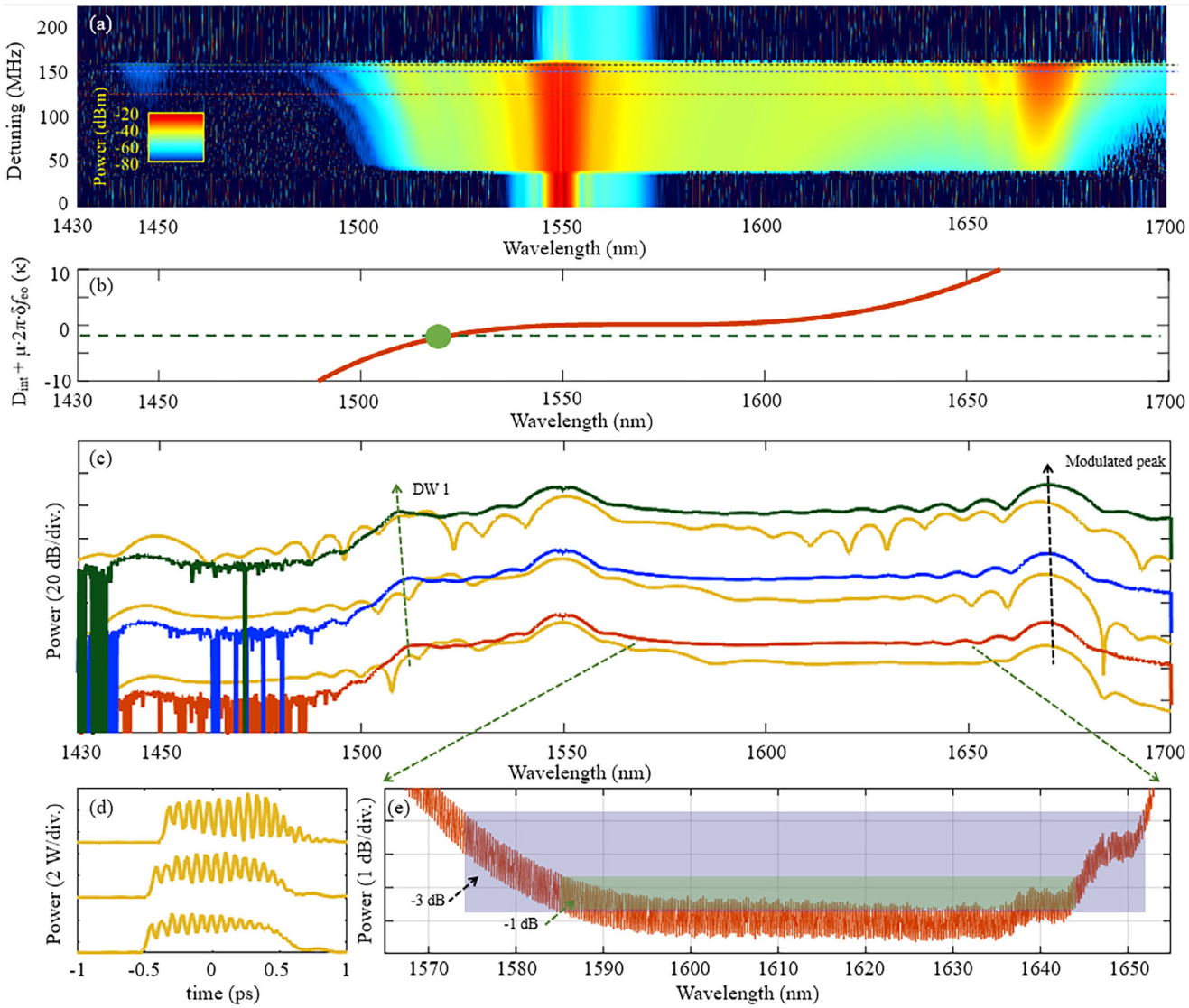

Figure 3. The evolution of spectra during the formation of the BS: a) Experimental spectrum evolution versus detuning. b) $D_{int}+\mu\cdot 2\pi\bullet\delta f_{eo}$ profile curve to determine the position of DW 1. The green dot indicates the DW 1 position of the line in c). (c) Experimental spectra corresponding to the dotted lines in (a) (red, blue, and green represent 122.7, 146.2, and 157.8 MHz respectively, from bottom to top), green (purple) arrow indicates the movement direction of DW 1 (modulated peak). (resolution of OSA is 2 nm). (40 dB vertical offsets). The simulated spectra are indicated by yellow lines. d) Simulated temporal profile of BS corresponding to the yellow lines in (c). e) Detailed view of the ultra-flat region in (c). (resolution of OSA is 0.04 nm). The green/purple shaded areas in (e) indicate an ultra-flat −1 dB/−3 dB bandwidth.

5. Experimental Observation of SRS Amplified BS

Now we investigate the comb evolution when the SRS effect is enhanced. By changing the desynchronization frequency δf_{eo} from −10 to 5 kHz, a new DW can be generated near the Raman gain region and thus get amplified by the SRS effect. With the appearance of Stokes and anti-Stokes peaks, the spectrum can be further broadened. But the spectral flatness will be deteriorated consequently.

The optical field evolution of the F-P cavity is recorded during the scanning process when δf_{eo} is set to 5 kHz, as shown in **Figure** 4a. Similarly, the reflected light exhibited distinct step features (see Section S4, Supporting Information) corresponding to the appearance of a broad spectrum in Figure 4a. Figure 4c shows three spectra at the detuning values of 239.69, 415.08, and 520.3 MHz. When the detuning is set to 239.69 MHz (depicted by the red line), we can observe five distinct characteristic peaks (marked by the numbers 1–5): the anti-Stokes peak, DW 1 peak, DW 2 peak, the Stokes peak, and the modulated peak. As indicated by the red dot in Figure 4b, the position of DW 2 near1590 nm, can also be predicted using $D_{int}+\mu\cdot 2\pi\cdot\delta f_{eo} = 2\cdot\gamma\cdot P\cdot L\cdot \mathrm{FSR}\text{-}\delta\omega = \delta\omega_{\mathrm{eff}}$ (see Section S5, Supporting Information). The appearance of the Stokes light is attributed to the overlap between DW 2 and the broadband Raman gain region of

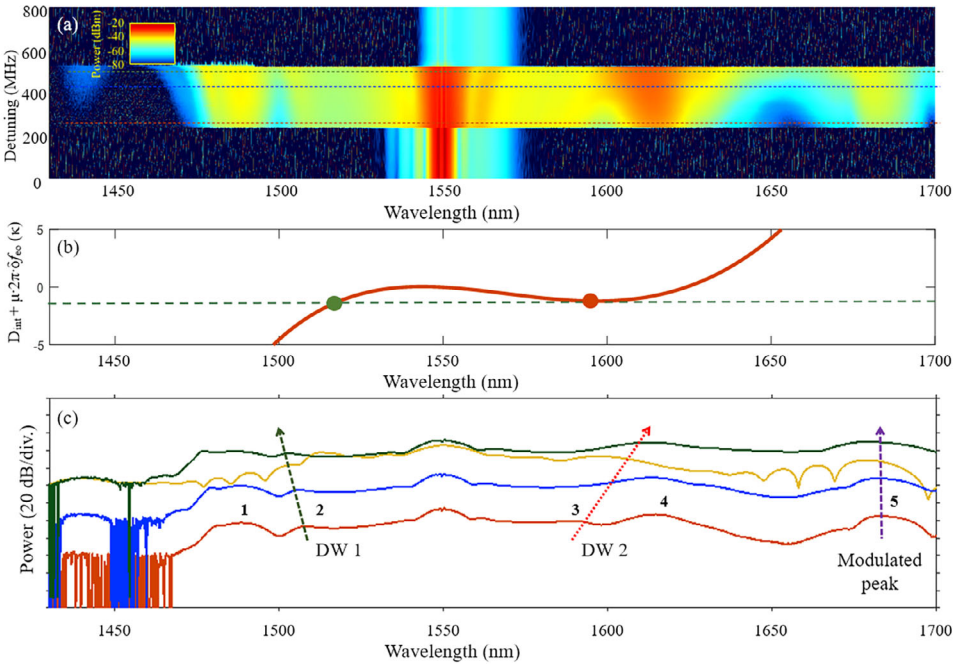

Figure 4. The evolution of spectra during the formation of the SRS-BS: a) Experimental spectrum evolution versus detuning. b) The $D_{int}+\mu\cdot 2\pi\cdot\delta f_{eo}$ profile curve used to determine the position of DW 1 and DW 2. The red (green) dot indicates the DW 2 (DW 1) position of the red line in (c). c) Experimental spectra corresponding to the dashed lines in (a) (red, blue, and green represent 239.69, 415.08, and 520.3 MHz respectively, from bottom to top), simulated spectrum (yellow line), the numbers 1–5 indicate anti-Stokes peak, DW 1, DW 2, Stokes peak and modulated peak. The red (green, purple) arrow indicates the movement direction of DW 2 (DW 1, modulated peak). (40 dB vertical offsets).

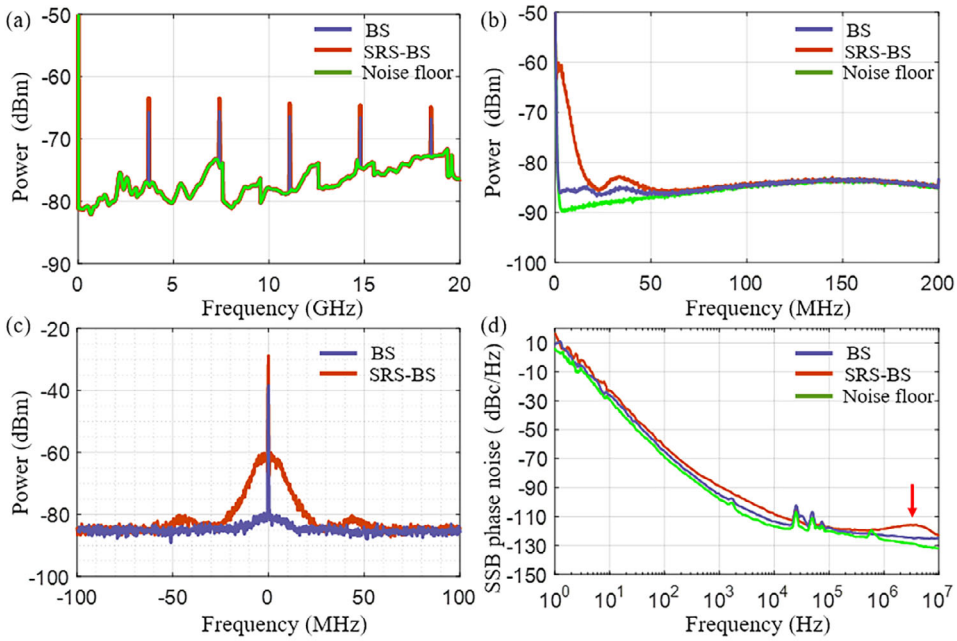

Figure 5. The noise characteristics of the SRS-BS and BS. a) Beatnote of the SRS-BS (red line) and BS (blue line) spectrum detected by a 40-GHz PD. b) Low-frequency noise of SRS-BS (red line), BS (blue line), and noise floor (green line). c) Beatnote signals (*f*-3.695923 GHz) of SRS-BS (red) and BS (blue) near 1520 nm (resolution bandwidth 100 kHz). d) Single sideband (SSB) phase noise spectra of SRS-BS (red), BS (blue), and pump light (green).

erbium-doped fiber (~1612 nm). This overlap satisfies the phase-matching condition of SRS. The anti-Stokes light is generated by the FWM between the pump light and the Stokes light. Due to the influence of TOD, the modulated peak still exists.

As the detuning increases to 415.08 and 520.3 MHz, DW 2 shifts toward longer wavelengths (see red arrow in Figure 4c), aligning with the Stokes light. Additionally, there is a noticeable increase in power for all peaks, particularly the modulated peak, which slowly shifts to the short wavelength position (indicated by the purple arrow in Figure 4c). While the SRS-BS spectrum (green line in Figure 4c) experiences a decrease in flatness compared to the above-mentioned BS spectrum, it exhibits a -30 dB bandwidth expansion from 190 to 230 nm (from 1470 to 1700 nm), and the number of comb lines exceeds 7700. The position of the modulated peak can be slightly adjusted by changing δf_{eo} to improve the flatness (see Section S6, Supporting Information). As shown in **Figure 5a**, the beatnotes of the BS spectrum (blue line) or SRS-BS spectrum (red line) demonstrate a single repetition frequency of 3.6959 GHz and its harmonics. This observation suggests that all the comb lines belong to the same mode family.

To further investigate the low-frequency noise characteristics of the BS spectrum (red line in Figure 3c) and the SRS-BS spectrum (green line in Figure 4c), both spectra are fed into an APD with a bandwidth of 200 MHz. The BS spectrum noise (blue line in Figure 5b) follows the noise floor (green line in Figure 5b), while the SRS-BS combs (red line in Figure 5b) exhibit higher noise levels compared to the BS comb in the 0–20 MHz range. Similar noise properties have also been reported in previous work.[64] In order to analyze the repetition frequency noise characteristics further, a portion of the comb light is filtered using a bandpass filter with a center wavelength of 1520 nm and a bandwidth of 40 nm. The filtered light is then amplified using an EDFA. The beatnote is measured using a 40 GHz photodetector (FINISAR) and analyzed using ESA. The results in Figure 5c indicate that the signal-to-noise ratio (SNR) is 30 dB for the SRS-BS comb and 50 dB for the BS comb. An increase in noise within a 20 MHz offset can be observed in the SRS-BS spectrum. The single-sideband phase noise spectra of the beat note signal are depicted in Figure 5d. In the frequency range of 1 MHz, the noise levels of the SRS-BS spectrum are −89 dBc Hz^{-1} at 1 kHz and −109 dBc Hz^{-1} at 10 kHz. This indicates ≈5 dB degradation compared to the BS spectrum. The SRS-BS spectrum displays a noise bump that is ≈9.5 dB higher than the BS spectrum, as represented by the red arrow in Figure 5d. This noise can be attributed to the noise of Raman amplification. Nonetheless, the noise levels of the BS or the SRS-BS spectrum remain comparable to our recent research on solitons in a near-zero-dispersion FP cavity.[68]

6. Conclusion

We have achieved an ultra-flat, broadband, and low-noise frequency comb with a −1 dB bandwidth up to 58 nm, corresponding to more than 1800 comb lines for a repetition rate of 3.69 GHz. The performance of our work is compared with other works in normal GVD microcavities, as shown in Appendix B. It can be observed that the generated comb spectrum has the largest −1 dB bandwidth (several times more than other works). The key to obtaining such an ultra-flat comb spectrum is to balance the platicon shape from normal GVD and the oscillatory spectrum from TOD. Moreover, by tuning the desynchronization frequency, which modifies the phase-matching condition for SRS, the influence of SRS can be manually controlled. With enhanced SRS, the comb spectrum can be further expanded due to the appearance of Stokes and anti-Stokes light. The −30 dB bandwidth is increased from 190 to 230 nm at a cost of reduced spectrum flatness. Our research work provides a novel route to obtain low-noise comb with ultra-flat and broadband spectrum. The desynchronization method is also demonstrated to be a powerful tool to flexibly control the influence of SRS and can stimulate research on the interaction between SRS and various effects in high-Q resonators.

Appendix A: Values of parameters measured in the experiment and used in the simulation.

Parameter	Experimentally measured values or given values by other work	Values used in simulation
$D_2/2\pi$ (β_2)	−28.2±3 Hz (1.6 ps^2/km)	−31.7 Hz (1.8 ps^2/km)
$D_3/2\pi$ (β_3)	−44.8±5 mHz 0.1095 ps^3/km	−48.29 mHz 0.118 ps^3/km
γ	10.8 $W^{-1}\cdot km^{-1}$	10.8 $W^{-1}\cdot km^{-1}$
$\kappa/2\pi$	19 MHz	17 MHz
P_0	14.4 W	13 W
τ_p	1.14 ps	1.1 ps
δf_{eo}	−10 or 5 kHz	−10 or 5 kHz
τ_1	12.2 fs	12.2 fs
τ_2	32 fs	32 fs
f_R	0.21	0.21

Appendix B: Performance comparison with other experimental works in normal GVD microcavities.

Platform	Repetition Rate	−1 dB Bandwidth
Fiber ring[48]	3.73 MHz	2 nm
Fiber ring[44]	8.4 MHz	5 nm
Fiber ring[4]	540 MHz	30 nm
Fiber F-P[62]	1.6 GHz	8 nm
Si_3N_4 microring[11]	14 GHz	10 nm
Si_3N_4 microring[29]	19 GHz	10 nm
Si_3N_4 microring[45]	27.88 GHz	20 nm
Si_3N_4 microring[36]	115.56 GHz	12 nm
Si_3N_4 microring[31]	227.33 GHz	10 nm
Fiber F-P This work	3.69 GHz	58 nm

Supporting Information

Supporting Information is available from the Wiley Online Library or from the author.

Acknowledgements

This work is supported by the National Nature Science Foundation of China (NSFC) (No. 61922056).

Conflict of Interest

The authors declare no conflict of interest.

Data Availability Statement

The data that support the findings of this study are available from the corresponding author upon reasonable request.

Keywords

dissipative Kerr solitons, F-P resonator, microcombs, nonlinear optics, stimulated Raman scattering

Received: February 3, 2024
Revised: October 1, 2024
Published online: January 31, 2025

[1] F. Leo, S. Coen, P. Kockaert, S.-P. Gorza, P. Emplit, M. Haelterman, *Nat. Photonics* **2010**, *4*, 471.
[2] T. Herr, V. Brasch, J. D. Jost, C. Y. Wang, N. M. Kondratiev, M. L. Gorodetsky, T. J. Kippenberg, *Nat. Photonics* **2013**, *8*, 145.
[3] N. Englebert, C. Mas Arabí, P. Parra-Rivas, S.-P. Gorza, F. Leo, *Nat. Photonics* **2021**, *15*, 536.
[4] Y. Xu, A. Sharples, J. Fatome, S. Coen, M. Erkintalo, S. G. Murdoch, *Opt. Lett.* **2021**, *46*, 512.
[5] C. Spiess, Q. Yang, X. Dong, V. G. Bucklew, W. H. Renninger, *Optica* **2021**, *8*, 861.
[6] C. Qin, K. Jia, Q. Li, T. Tan, X. Wang, Y. Guo, S.-W. Huang, Y. Liu, S. Zhu, Z. Xie, Y. Rao, B. Yao, *Light: Sci. Appl.* **2020**, *9*, 185.
[7] E. Obrzud, S. Lecomte, T. Herr, *Nat. Photonics* **2017**, *11*, 600.
[8] K. Jia, X. Wang, D. Kwon, J. Wang, E. Tsao, H. Liu, X. Ni, J. Guo, M. Yang, X. Jiang, J. Kim, S. N. Zhu, Z. Xie, S. W. Huang, *Phys. Rev. Lett.* **2020**, *125*, 143902.
[9] C. Qin, J. Du, T. Tan, B. Chang, K. Jia, Y. Liang, W. Wang, Y. Guo, H. Xia, S. Zhu, Y. Rao, Z. Xie, B. Yao, *Laser Photonics Rev.* **2023**, *17*, 2200662.
[10] M. H. Anderson, R. Bouchand, J. Liu, W. Weng, E. Obrzud, T. Herr, T. J. Kippenberg, *Optica* **2021**, *8*, 771.
[11] Z. Ye, F. Lei, K. Twayana, M. Girardi, P. A. Andrekson, V. Torres-Company, *Laser Photonics Rev.* **2022**, *16*, 2100147.
[12] A. G. Griffith, R. K. W. Lau, J. Cardenas, Y. Okawachi, A. Mohanty, R. Fain, Y. H. D. Lee, M. Yu, C. T. Phare, C. B. Poitras, A. L. Gaeta, M. Lipson, *Nat. Commun.* **2015**, *6*, 6299.
[13] X. Yi, Q.-F. Yang, K. Y. Yang, M.-G. Suh, K. Vahala, *Optica* **2015**, *2*, 1078.
[14] D. Jeong, D. Kwon, I. Jeon, I. H. Do, J. Kim, H. Lee, *Optica* **2020**, *7*.
[15] Y. He, Q.-F. Yang, J. Ling, R. Luo, H. Liang, M. Li, B. Shen, H. Wang, K. Vahala, Q. Lin, *Optica* **2019**, *6*, 1138.
[16] Z. Gong, X. Liu, Y. Xu, H. X. Tang, *Optica* **2020**, *7*, 1275.
[17] C. Yang, S. Yang, F. Du, X. Zeng, B. Wang, Z. Yang, Q. Luo, R. Ma, R. Zhang, D. Jia, Z. Hao, Y. Li, Q. Yang, X. Yi, F. Bo, Y. Kong, G. Zhang, J. Xu, *Laser Photonics Rev.* **2023**, *17*, 2200510.
[18] X. Liu, Z. Gong, A. W. Bruch, J. B. Surya, J. Lu, H. X. Tang, *Nat. Commun.* **2021**, *12*, 5428.
[19] H. Weng, J. Liu, A. A. Afridi, J. Li, J. Dai, X. Ma, Y. Zhang, Q. Lu, J. F. Donegan, W. Guo, *Photon. Res.* **2021**, *9*.
[20] G. Moille, L. Chang, W. Xie, A. Rao, X. Lu, M. Davanço, J. E. Bowers, K. Srinivasan, *Laser Photonics Rev.* **2020**, *14*, 2000022.
[21] C. Godey, I. V. Balakireva, A. Coillet, Y. K. Chembo, *Phys. Rev. A* **2014**, *89*.
[22] J. Li, C. Bao, Q.-X. Ji, H. Wang, L. Wu, S. Leifer, C. Beichman, K. Vahala, *Optica* **2022**, *9*, 231.
[23] X. Xue, P.-H. Wang, Y. Xuan, M. Qi, A. M. Weiner, *Laser Photonics Rev.* **2017**, *11*, 1600276.
[24] H. Zhou, Y. Geng, W. Cui, S. W. Huang, Q. Zhou, K. Qiu, C. W. Wong, *Light: Sci. Appl.* **2019**, *8*, 50.
[25] H. Guo, M. Karpov, E. Lucas, A. Kordts, M. H. P. Pfeiffer, V. Brasch, G. Lihachev, V. E. Lobanov, M. L. Gorodetsky, T. J. Kippenberg, *Nat. Phys.* **2016**, *13*, 94.
[26] Y. Zhao, L. Chen, C. Zhang, W. Wang, H. Hu, R. Wang, X. Wang, S. T. Chu, B. Little, W. Zhang, X. Zhang, *Laser Photonics Rev.* **2021**, *15*, 2100264.
[27] P. Parra-Rivas, D. Gomila, E. Knobloch, S. Coen, L. Gelens, *Opt. Lett.* **2016**, *41*, 2402.
[28] P. Parra-Rivas, D. Gomila, L. Gelens, *Phys. Rev. A* **2017**, *95*, 053863.
[29] H. Liu, S.-W. Huang, W. Wang, J. Yang, M. Yu, D.-L. Kwong, P. Colman, C. W. Wong, *Photon. Res.* **2022**, *10*, 1877.
[30] G. Lihachev, W. Weng, J. Liu, L. Chang, J. Guo, J. He, R. N. Wang, M. H. Anderson, Y. Liu, J. E. Bowers, T. J. Kippenberg, *Nat. Commun.* **2022**, *13*, 1771.
[31] Ó. B. Helgason, F. R. Arteaga-Sierra, Z. Ye, K. Twayana, P. A. Andrekson, M. Karlsson, J. Schröder, T.-C. Victor, *Nat. Photonics* **2021**, *15*, 305.
[32] C. Bao, Y. Xuan, C. Wang, A. Fülöp, D. E. Leaird, V. Torres-Company, M. Qi, A. M. Weiner, *Phys. Rev. Lett.* **2018**, *121*, 257401.
[33] J. K. Jang, Y. Okawachi, M. Yu, K. Luke, X. Ji, M. Lipson, A. L. Gaeta, *Opt. Express* **2016**, *24*, 28794.
[34] X. Xue, Y. Xuan, P.-H. Wang, Y. Liu, D. E. Leaird, M. Qi, A. M. Weiner, *Laser Photonics Rev.* **2015**, *9*, L23.
[35] X. Xue, Y. Xuan, Y. Liu, P.-H. Wang, S. Chen, J. Wang, D. E. Leaird, M. Qi, A. M. Weiner, *Nat. Photonics* **2015**, *9*, 594.
[36] S. W. Huang, H. Zhou, J. Yang, J. F. McMillan, A. Matsko, M. Yu, D. L. Kwong, L. Maleki, C. W. Wong, *Phys. Rev. Lett.* **2015**, *114*, 053901.
[37] Y. Liu, Y. Xuan, X. Xue, P.-H. Wang, S. Chen, A. J. Metcalf, J. Wang, D. E. Leaird, M. Qi, A. M. Weiner, *Optica* **2014**, *1*, 137.
[38] W. Liang, A. A. Savchenkov, V. S. Ilchenko, D. Eliyahu, D. Seidel, A. B. Matsko, L. Maleki, *Opt. Lett.* **2014**, *39*, 2920.
[39] B. Y. Kim, Y. Okawachi, J. K. Jang, M. Yu, X. Ji, Y. Zhao, C. Joshi, M. Lipson, A. L. Gaeta, *Opt. Lett.* **2019**, *44*, 4475.
[40] V. E. Lobanov, G. Lihachev, T. J. Kippenberg, M. L. Gorodetsky, *Opt. Express* **2015**, *23*, 7713.
[41] V. E. Lobanov, A. E. Shitikov, R. R. Galiev, K. N. Min'kov, O. V. Borovkova, N. M. Kondratiev, *Phys. Rev. A* **2021**, *104*, 063511.
[42] V. E. Lobanov, N. M. Kondratiev, A. E. Shitikov, R. R. Galiev, I. A. Bilenko, *Phys. Rev. A* **2019**, *100*, 013807.
[43] S. Zhang, T. Bi, P. Del'Haye, *Laser Photonics Rev.* **2023**, *17*, 2300075.
[44] Z. Li, Y. Xu, S. Coen, S. G. Murdoch, M. Erkintalo, *Optica* **2020**, *7*, 1195.
[45] M. H. Anderson, W. Weng, G. Lihachev, A. Tikan, J. Liu, T. J. Kippenberg, *Nat. Commun.* **2022**, *13*, 4764.
[46] M.-G. Suh, K. Vahala, *Optica* **2018**, *5*, 65.

[47] L. Yao, P. Liu, H.-J. Chen, Q. Gong, Q.-F. Yang, Y.-F. Xiao, *Optica* **2022**, *9*, 561.
[48] X. Xue, P. Grelu, B. Yang, M. Wang, S. Li, X. Zheng, B. Zhou, *Light: Sci. Appl.* **2023**, *12*, 19.
[49] X. Wang, X. Qiu, M. Liu, F. Liu, M. Li, L. Xue, B. Chen, M. Zhang, P. Xie, *Opto-Electron. Sci.* **2023**, *2*, 230024.
[50] W. Liang, V. S. Ilchenko, A. A. Savchenkov, A. B. Matsko, D. Seidel, L. Maleki, *Phys. Rev. Lett.* **2010**, *105*, 143903.
[51] Z. Li, Q. Du, C. Wang, J. Zou, T. Du, K. A. Richardson, Z. Cai, J. Hu, Z. Luo, *Laser Photonics Rev.* **2021**, *15*, 2000301.
[52] Y. K. Chembo, I. S. Grudinin, N. Yu, *Phys. Rev. A* **2015**, *92*, 043818.
[53] S. Yao, C. Bao, P. Wang, C. Yang, *Phys. Rev. A* **2020**, *101*, 023833.
[54] G. Lin, Q. Song, *Laser Photonics Rev.* **2022**, *16*, 2100184.
[55] X. Yi, Q.-F. Yang, K. Y. Yang, K. Vahala, *Opt. Lett.* **2016**, *41*, 3419.
[56] C. Milián, A. V. Gorbach, M. Taki, A. V. Yulin, D. V. Skryabin, *Phys. Rev. A* **2015**, *92*, 033851.
[57] M. Karpov, H. Guo, A. Kordts, V. Brasch, M. H. P. Pfeiffer, M. Zervas, M. Geiselmann, T. J. Kippenberg, *Phys. Rev. Lett.* **2016**, *116*, 103902.
[58] Y. Wang, M. Anderson, S. Coen, S. G. Murdoch, M. Erkintalo, *Phys. Rev. Lett.* **2018**, *120*, 053902.
[59] Q.-F. Yang, X. Yi, K. Y. Yang, K. Vahala, *Nat. Phys.* **2016**, *13*, 53.
[60] T. Tan, Z. Yuan, H. Zhang, G. Yan, S. Zhou, N. An, B. Peng, G. Soavi, Y. Rao, B. Yao, *Nat. Commun.* **2021**, *12*, 6716.
[61] A. V. Cherenkov, N. M. Kondratiev, V. E. Lobanov, A. E. Shitikov, D. V. Skryabin, M. L. Gorodetsky, *Opt. Express* **2017**, *25*, 31148.
[62] Z. Li, Y. Xu, S. Shamailov, X. Wen, W. Wang, X. Wei, Z. Yang, S. Coen, S. G. Murdoch, M. Erkintalo, *Nat. Photonics* **2024**, *18*, 46.
[63] P. Parra-Rivas, S. Coulibaly, M. G. Clerc, M. Tlidi, *Phys. Rev. A* **2021**, *103*, 013507.
[64] T. Li, K. Wu, X. Zhang, M. Cai, J. Chen, *Optica* **2023**, *10*, 1389.
[65] H. Zhang, T. Tan, H.-J. Chen, Y. Yu, W. Wang, B. Chang, Y. Liang, Y. Guo, H. Zhou, H. Xia, Q. Gong, C. W. Wong, Y. Rao, Y.-F. Xiao, B. Yao, *Phys. Rev. Lett.* **2023**, *130*, 153802.
[66] Y. Xu, Y. Lin, A. Nielsen, I. Hendry, S. Coen, M. Erkintalo, H. Ma, S. G. Murdoch, *Optica* **2020**, *7*.
[67] D. C. Cole, A. Gatti, S. B. Papp, F. Prati, L. Lugiato, *Phys. Rev. A* **2018**, *98*, 013831.
[68] Z. Xiao, T. Li, M. Cai, H. Zhang, Y. Huang, C. Li, B. Yao, K. Wu, J. Chen, *Light: Sci. Appl.* **2023**, *12*, 33.